Available online at www.sciencedirect.com
ScienceDirect
Journal of Computational Physics 218 (2006) 794–815
JOURNAL OF COMPUTATIONAL PHYSICS
www.elsevier.com/locate/jcp

An artificial compressibility flux for the discontinuous Galerkin solution of the incompressible Navier–Stokes equations

F. Bassi [a,*], A. Crivellini [a], D.A. Di Pietro [a], S. Rebay [b]

[a] *Dipartimento di Ingegneria Industriale, Università di Bergamo, via Marconi 4, 24044 Dalmine (BG), Italy*
[b] *Dipartimento di Ingegneria Meccanica, Università di Brescia, via Branze 38, 25123 Brescia, Italy*

Received 6 July 2005; received in revised form 8 March 2006; accepted 9 March 2006
Available online 25 April 2006

Abstract

Discontinuous Galerkin (DG) methods have proved to be well suited for the construction of robust high-order numerical schemes on unstructured and possibly nonconforming grids for a variety of problems. Their application to the incompressible Navier–Stokes (INS) equations has also been recently considered, although the subject is far from being fully explored. In this work, we propose a new approach for the DG numerical solution of the INS equations written in conservation form. The inviscid numerical fluxes both in the continuity and in the momentum equation are computed using the values of velocity and pressure provided by the (exact) solution of the Riemann problem associated with a local artificial compressibility perturbation of the equations. Unlike in most of the existing methods, artificial compressibility is here introduced only at the interface flux level, therefore resulting in a consistent discretization of the INS equations irrespectively of the amount of artificial compressibility introduced. The discretization of the viscous term follows the well-established DG scheme named BR2. The performance and the accuracy of the method are demonstrated by computing the Kovasznay flow and the two-dimensional lid-driven cavity flow for a wide range of Reynolds numbers and for various degrees of polynomial approximation.

PACS: 47.10.ad; 47.11.Fg

Keywords: Incompressible Navier–Stokes equations; Discontinuous Galerkin methods; Artificial compressibility; Riemann solver

1. Introduction

Discontinuous Galerkin (DG) methods have proved to be suited for the construction of robust high-order numerical schemes on arbitrary unstructured and possibly nonconforming grids for a wide variety of problems. The application of the DG space discretization to incompressible fluid flows has also been considered

* Corresponding author.
E-mail addresses: francesco.bassi@unibg.it (F. Bassi), andrea.crivellini@unibg.it (A. Crivellini), dipietro@unibg.it (D.A. Di Pietro), stefano.rebay@ing.unibs.it (S. Rebay).

0021-9991/$ - see front matter
doi:10.1016/j.jcp.2006.03.006

in a few recent works. In [1], Liu and Shu introduce a DG method for 2D incompressible flows in stream function formulation, whereby the DG approximation is applied to the momentum equation, while a continuous finite element approximation of the stream function is computed by a standard Poissons solver. In a series of papers [2–4] Cockburn and coworkers propose and thoroughly analyze the local discontinuous Galerkin (LDG) method for the Stokes, Oseen and INS equations respectively. In all cases, the problem is discretized using a fully discontinuous approach and the authors propose expressions of the numerical fluxes associated with the Laplacian and the incompressibility constraint, which are based on analogous recipes. In this paper, we also apply the DG discretization to the primitive variable form of the INS equations, but we introduce a novel formulation of the inviscid numerical flux, which relies on the solution of a Riemann problem for the incompressible Euler equations with a suitably relaxed incompressibility constraint.

One of the key ingredients of DG methods is the formulation of interface (numerical) fluxes, which provide a weak coupling between the unknowns in neighbouring elements. In the inviscid compressible case, the numerical flux is often computed by exploiting the hyperbolic nature of the equations as the (approximate or exact) solution of a Riemann problem. In the incompressible case, however, the equations are no longer hyperbolic due to the lack of the unsteady term in the continuity equation and it is therefore not possible to compute the interface flux following the same approach. In this paper, we circumvent this difficulty by adding an *artificial compressibility term* to the continuity equation so as to recover the hyperbolic nature of the problem. The flux computation can then mimic the procedure followed in the compressible case.

The idea of relaxing the incompressibility constraint by adding an artificial compressibility term has been known for a long time and has been extensively used in finite volume as well as in finite element approximations of the INS equations. It is important to remark that this old idea is here exploited in a new way in that it is deployed *only* for the construction of the interface fluxes. This entails that the DG discretization here introduced is always a strongly consistent approximation of the INS equations since, independently of the amount of artificial compressibility added, the interface flux reduces to the physical one for vanishing interface jumps. The numerical experiments show indeed a limited dependence of the computed solution from the amount of artificial compressibility introduced.

To complete the DG space discretization of the INS equations we follow the same approach introduced in [5] for the compressible viscous case, i.e. we handle the viscous term separately and for its discretization we use the well established DG BR2 scheme introduced in [6] and referred to as BRMPS in [7]. A complete survey and analysis of DG methods for elliptic problems can be found therein. Finally, the semi-discrete equations are integrated in time with a fully implicit method.

The numerical results presented below show that the inviscid and viscous interface fluxes here proposed provide a stabilization of the discretized form of the INS problem, which allows for high Reynolds number computations and equal order approximation. The performance of the proposed method is demonstrated by computing several classical test cases for a wide range of Reynolds numbers: thorough testing has been done on Kovasznay's analytical solutions of the Navier–Stokes equations (see [8]), and on the lid-driven cavity flow problem for Reynolds number up to 20,000 (see [9–11]).

The paper is organized as follows: in Section 2 we describe the DG discretization of the INS equations; in Section 3 we discuss some implementation issues; Section 4 is devoted to the numerical results and Section 5 to the conclusions. The derivation of the exact solution of the Riemann problem for the incompressible Navier–Stokes, Oseen and Stokes equations perturbed by artificial compressibility is thoroughly described in Appendix A.

2. DG approximation of the incompressible Navier–Stokes equations

The incompressible Navier–Stokes equations read

$$\begin{aligned} &\frac{\partial \mathbf{u}}{\partial t} - \nabla \cdot (\nu \nabla \mathbf{u}) + \mathbf{u} \cdot \nabla \mathbf{u} + \nabla p = \mathbf{g}, \\ &\nabla \cdot \mathbf{u} = 0, \end{aligned} \tag{1}$$

in $[0,t]\times\Omega$, $\Omega \subset \mathbb{R}^N$, where $N \in \{2,3\}$ is the number of space dimensions, $\mathbf{u}$ denotes the velocity vector and $p = P/\rho$ is the pressure divided by the density. For the sake of simplicity, we assume that Dirichlet boundary conditions for the velocity $\mathbf{u}$ are prescribed on the boundary, i.e.

$$\mathbf{u} = \mathbf{f} \quad \text{on } \partial\Omega. \tag{2}$$

By virtue of the incompressibility constraint, the momentum equation can be alternatively written in conservation form as

$$\frac{\partial \mathbf{u}}{\partial t} - \boldsymbol{\nabla} \cdot (\nu \boldsymbol{\nabla} \mathbf{u}) + \boldsymbol{\nabla} \cdot \mathbf{F}(\mathbf{u}, p) = \mathbf{g}, \tag{3}$$

where the flux $\mathbf{F}(\mathbf{u},p)$ is given by

$$\mathbf{F}(\mathbf{u},p) \stackrel{\text{def}}{=} \mathbf{u} \otimes \mathbf{u} + p\mathbf{I} = u_i u_j + p\delta_{ij}.$$

2.1. Incompressible Euler equations

We proceed as discussed in the introduction by treating the viscous and inviscid parts independently. We first consider the space discretization of the inviscid incompressible Navier–Stokes (or incompressible Euler) equations

$$\begin{aligned} &\frac{\partial \mathbf{u}}{\partial t} + \boldsymbol{\nabla} \cdot \mathbf{F}(\mathbf{u}, p) = \mathbf{g}, \\ &\boldsymbol{\nabla} \cdot \mathbf{u} = 0. \end{aligned} \tag{4}$$

The weak form of the incompressible Euler equations reads: find $(\mathbf{u},p) \in [H^1(\Omega)]^N \times L^2(\Omega)$ such that

$$\begin{aligned} &\int_\Omega \mathbf{v} \cdot \frac{\partial \mathbf{u}}{\partial t} \,\mathrm{d}\mathbf{x} - \int_\Omega \boldsymbol{\nabla}\mathbf{v} : \mathbf{F}(\mathbf{u}, p) \,\mathrm{d}\mathbf{x} + \int_{\partial\Omega} \mathbf{v} \otimes \mathbf{n} : \mathbf{F}(\mathbf{u}, p) \,\mathrm{d}\sigma = \int_\Omega \mathbf{v} \cdot \mathbf{g} \,\mathrm{d}\mathbf{x}, \\ &\int_\Omega q \boldsymbol{\nabla} \cdot \mathbf{u} \,\mathrm{d}\mathbf{x} = 0 \end{aligned} \tag{5}$$

for all $(\mathbf{v}, q) \in [H^1(\Omega)]^N \times L^2(\Omega)$.

In order to construct a DG discretization of Eq. (5), we consider a triangulation $\mathscr{T}_h = \{K\}$ of an approximation Ω_h of Ω, that is we partition Ω_h into a set of non-overlapping elements K (not necessarily simplices). We denote with $\mathscr{E}_h^0$ the set of internal element faces, with $\mathscr{E}_h^\partial$ the set of boundary element faces and with $\mathscr{E}_h = \mathscr{E}_h^0 \cup \mathscr{E}_h^\partial$ their union. We moreover set

$$\Gamma_h^0 = \bigcup_{e \in \mathscr{E}_h^0} e, \qquad \Gamma_h^\partial = \bigcup_{e \in \mathscr{E}_h^\partial} e, \qquad \Gamma_h = \Gamma_h^0 \cup \Gamma_h^\partial. \tag{6}$$

The solution is approximated on $\mathscr{T}_h$ as a piecewise polynomial function possibly discontinuous on element interfaces, i.e. we assume the following space settings for the approximate solution $\mathbf{u}_h$ and p_h:

$$\mathbf{u}_h \in \mathbf{V}_h \stackrel{\text{def}}{=} [V_h]^N, \qquad p_h \in Q_h \stackrel{\text{def}}{=} V_h, \tag{7}$$

with

$$V_h \stackrel{\text{def}}{=} \left\{ v_h \in L^2(\Omega) : v_h|_K \in \mathbb{P}_k(K) \ \forall K \in \mathscr{T}_h \right\}$$

for some polynomial order $k \geqslant 1$, being $\mathbb{P}_k(K)$ the space of polynomials of global degree at most k on the element K.

In order to simplify the presentation, it is convenient to introduce some trace operators which generalize those defined in [7]. On a generic internal face $e \in \mathscr{E}_h^0$, see Fig. 1, we define

$$\begin{aligned} &[\![\mathbf{v}]\!] \stackrel{\text{def}}{=} \mathbf{v}^+ \otimes \mathbf{n}^+ + \mathbf{v}^- \otimes \mathbf{n}^-, \qquad [\![q]\!] \stackrel{\text{def}}{=} q^+ \mathbf{n}^+ + q^- \mathbf{n}^-, \\ &[q] \stackrel{\text{def}}{=} q^+ - q^-, \qquad \{q\} \stackrel{\text{def}}{=} \frac{q^+ + q^-}{2}, \end{aligned} \tag{8}$$

where $\mathbf{v}$ denotes a generic vector quantity and q a generic scalar quantity. Notice that $[\![\mathbf{v}]\!]$ is a tensor quantity, and $[\![q]\!]$ is a vector quantity, i.e. this operator always increases the tensor rank by one. These definitions can be

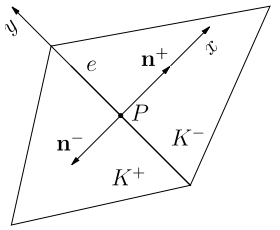

Fig. 1. Normals and local frame at quadrature point P on edge e.

suitably extended to faces intersecting $\partial\Omega$ accounting for the weak imposition of the Dirichlet datum. The weak imposition of boundary conditions is discussed in Section 3.3.

The discrete counterpart of Eq. (5) for a generic element $K \in \mathscr{T}_h$ then reads

$$\begin{aligned}&\int_K \mathbf{v}_h \cdot \frac{\partial \mathbf{u}_h}{\partial t}\,\mathrm{d}\mathbf{x} - \int_K \nabla_h \mathbf{v}_h : \mathbf{F}(\mathbf{u}_h, p_h)\,\mathrm{d}\mathbf{x} + \int_{\partial K} \mathbf{v}_h \otimes \mathbf{n} : \mathbf{F}(\mathbf{u}_h|_K, p_h|_K)\,\mathrm{d}\sigma = \int_K \mathbf{v}_h \cdot \mathbf{g}\,\mathrm{d}\mathbf{x},\\ &- \int_K \nabla_h q_h \cdot \mathbf{u}_h\,\mathrm{d}\mathbf{x} + \int_{\partial K} q_h \mathbf{u}_h|_K \cdot \mathbf{n}\,\mathrm{d}\sigma = 0,\end{aligned} \tag{9}$$

where we integrated by parts the continuity equation. To introduce a coupling between the degrees of freedom belonging to adjacent elements and to ensure conservation, we substitute the fluxes $\mathbf{F}(\mathbf{u}_h|_K, p_h|_K)$ and $\mathbf{u}_h|_K$ with suitably defined numerical fluxes $\widehat{\mathbf{F}}(\mathbf{u}_h^+, p_h^+; \mathbf{u}_h^-, p_h^-)$ and $\hat{\mathbf{u}}(\mathbf{u}_h^+, p_h^+; \mathbf{u}_h^-, p_h^-)$. The stability and accuracy properties of the method strongly depend on the choice of such numerical fluxes, which is therefore of great importance.

Summing Eq. (9) over the elements we obtain the DG formulation of problem (5) which then requires to find $(\mathbf{u}_h, p_h) \in \mathbf{V}_h \times Q_h$ such that

$$\begin{aligned}&\int_{\Omega_h} \mathbf{v}_h \cdot \frac{\partial \mathbf{u}_h}{\partial t}\,\mathrm{d}\mathbf{x} - \int_{\Omega_h} \nabla_h \mathbf{v}_h : \mathbf{F}(\mathbf{u}_h, p_h)\,\mathrm{d}\mathbf{x} + \int_{\Gamma_h} [\![\mathbf{v}_h]\!] : \widehat{\mathbf{F}}(\mathbf{u}_h^+, p_h^+; \mathbf{u}_h^-, p_h^-)\,\mathrm{d}\sigma = \int_{\Omega_h} \mathbf{v}_h \cdot \mathbf{g}\,\mathrm{d}\mathbf{x},\\ &- \int_{\Omega_h} \nabla_h q_h \cdot \mathbf{u}_h\,\mathrm{d}\mathbf{x} + \int_{\Gamma_h} [\![q_h]\!] \cdot \hat{\mathbf{u}}(\mathbf{u}_h^+, p_h^+; \mathbf{u}_h^-, p_h^-)\,\mathrm{d}\sigma = 0\end{aligned} \tag{10}$$

for all $(\mathbf{v}_h, q_h) \in \mathbf{V}_h \times Q_h$.

The key idea adopted to compute $\widehat{\mathbf{F}}$ and $\hat{\mathbf{u}}$ is to reduce the problem of flux computation to the solution of a planar Riemann problem as in the compressible case. In order to recover the hyperbolic character of the equations, the incompressibility constraint is relaxed by adding an artificial compressibility term to the continuity equation. At each quadrature point P on Γ_h we therefore solve the Riemann problem for the equations

$$\begin{aligned}&\frac{1}{c^2}\frac{\partial p}{\partial t} + \frac{\partial u}{\partial x} = 0,\\ &\frac{\partial u}{\partial t} + \frac{\partial (u^2 + p)}{\partial x} = 0,\\ &\frac{\partial v}{\partial t} + \frac{\partial uv}{\partial x} = 0,\end{aligned} \tag{11}$$

with initial datum

$$(\mathbf{u}, p) = \begin{cases} (\mathbf{u}_h^-, p_h^-) & \text{if } x < 0,\\ (\mathbf{u}_h^+, p_h^+) & \text{if } x > 0,\end{cases}$$

with initial datum

$$(\mathbf{u}, p) = \begin{cases} (\mathbf{u}_h^-, p_h^-) & \text{if } x < 0,\\ (\mathbf{u}_h^+, p_h^+) & \text{if } x > 0,\end{cases}$$

where x denotes a locally defined axis oriented as the normal vector $\mathbf{n}^+$ pointing out of K^+ and located in such a way that $x = 0$ at P, see Fig. 1.

Denoting with $(\mathbf{u}_*, p_*)$ the solution of the Riemann problem on the space-time line $x/t = 0$, we finally set

$$\widehat{\mathbf{F}}(\mathbf{u}_h^+, p_h^+; \mathbf{u}_h^-, p_h^-) = \mathbf{F}(\mathbf{u}_*, p_*), \qquad \hat{\mathbf{u}}(\mathbf{u}_h^+, p_h^+; \mathbf{u}_h^-, p_h^-) = \mathbf{u}_*.$$

On boundary faces where the Dirichlet boundary conditions are prescribed the role of the variable on the exterior is played by the datum.

The procedure adopted for the determination of the state $(\mathbf{u}_*, p_*)$ is thoroughly discussed in Appendix A for the case of the incompressible Euler equations as well as for the Stokes and Oseen equations, which we consider for the purpose of comparison with existing methods. It is worth noticing that, unlike in [2–4], we do not split the numerical flux related to the advection term from that related to the pressure term, thus establishing a stronger link between pressure and velocity which seems to enhance the properties of the method. A detailed analysis of the method for the Stokes and Incompressible Euler problems has recently been made in [12, Chapters 4 and 5].

2.2. Navier–Stokes equations

Many techniques are available for the DG space discretization of the viscous term: a complete survey can be found in [7]. Several schemes can be traced back to the following general framework:

$$\int_{\Omega_h} \nu \nabla_h \mathbf{v}_h : \nabla_h \mathbf{u}_h \,\mathrm{d}\mathbf{x} - \int_{\Gamma_h} \nu(\llbracket \mathbf{v}_h \rrbracket : \{\nabla_h \mathbf{u}_h\} + \llbracket \mathbf{u}_h \rrbracket : \{\nabla_h \mathbf{v}_h\}) \,\mathrm{d}\sigma + \alpha(\mathbf{v}_h, \mathbf{u}_h), \tag{12}$$

where the boundary integral is in fact a consistency term and $\alpha(\cdot,\cdot)$ is a suitable penalty term. In this paper we choose the form of the penalty term first proposed in [6], which reads

$$\alpha(\mathbf{v}_h, \mathbf{u}_h) = \sum_{e \in \mathscr{E}_h} \eta_e \int_{\Omega_h} \nu \mathbf{r}_e(\llbracket \mathbf{v}_h \rrbracket) : \mathbf{r}_e(\llbracket \mathbf{u}_h \rrbracket) \,\mathrm{d}\mathbf{x},$$

where $\mathbf{r}_e : [L^2(e)]^{N^2} \to \Sigma_h$ is the lifting operator defined as the solution of the following problem:

$$\int_{\Omega_h} \mathbf{r}_e(\boldsymbol{\psi}) : \boldsymbol{\tau}_h \,\mathrm{d}\mathbf{x} = -\int_e \boldsymbol{\psi} : \{\boldsymbol{\tau}_h\} \,\mathrm{d}\sigma, \quad \forall \boldsymbol{\tau}_h \in \Sigma_h, \ \ \boldsymbol{\psi} \in [L^1(e)]^{N^2}, \tag{13}$$

e being a generic face and $\Sigma_h \overset{\text{def}}{=} [V_h]^{N^2}$. It is possible to find lower bounds for the parameter $\eta_e \in \mathbb{R}^+$ ensuring stability of the method. This form for the penalty term was obtained by first writing a mixed formulation for the elliptic term, choosing proper numerical fluxes and then eliminating the auxiliary variable. We refer the interested reader to [7] for the details.

Keeping in mind the discussion above, the space discretization of the incompressible Navier–Stokes equations reads: find $(\mathbf{u}_h, p_h) \in \mathbf{V}_h \times Q_h$ such that

$$\begin{aligned}
&\int_{\Omega_h} \mathbf{v}_h \cdot \frac{\partial \mathbf{u}_h}{\partial t} \,\mathrm{d}\mathbf{x} + \int_{\Omega_h} \nu \nabla_h \mathbf{v}_h : \nabla_h \mathbf{u}_h \,\mathrm{d}\mathbf{x} - \int_{\Gamma_h} \nu(\llbracket \mathbf{v}_h \rrbracket : \{\nabla_h \mathbf{u}_h\} + \llbracket \mathbf{u}_h \rrbracket : \{\nabla_h \mathbf{v}_h\}) \,\mathrm{d}\sigma + \alpha(\mathbf{v}_h, \mathbf{u}_h) \\
&\quad - \int_{\Omega_h} \nabla_h \mathbf{v}_h : \mathbf{F}(\mathbf{u}_h, p_h) \,\mathrm{d}\mathbf{x} + \int_{\Gamma_h} \llbracket \mathbf{v}_h \rrbracket : \widehat{\mathbf{F}}(\mathbf{u}_h^+, p_h^+; \mathbf{u}_h^-, p_h^-) \,\mathrm{d}\sigma = \int_{\Omega_h} \mathbf{v}_h \cdot \mathbf{g} \,\mathrm{d}\mathbf{x}, \\
&- \int_{\Omega_h} \nabla_h q_h \cdot \mathbf{u}_h \,\mathrm{d}\mathbf{x} + \int_{\Gamma_h} \llbracket q_h \rrbracket \cdot \hat{\mathbf{u}}(\mathbf{u}_h^+, p_h^+; \mathbf{u}_h^-, p_h^-) \,\mathrm{d}\sigma = 0
\end{aligned} \tag{14}$$

for all $(\mathbf{v}_h, q_h) \in \mathbf{V}_h \times Q_h$.

3. Implementation issues

In this section, we shall give some implementation details. We start by deriving a form of Eq. (14) which is closer to implementation. The viscous penalty term can be re-written as follows:

$$\alpha(\mathbf{v}_h, \mathbf{u}_h) = \sum_{e \in \mathscr{E}_h} \eta_e \int_{\Omega_h} \nu \mathbf{r}_e(\llbracket \mathbf{v}_h \rrbracket) : \mathbf{r}_e(\llbracket \mathbf{u}_h \rrbracket) \,\mathrm{d}\mathbf{x} = -\sum_{e \in \mathscr{E}_h} \eta_e \int_e \nu \llbracket \mathbf{v}_h \rrbracket : \{\mathbf{r}_e \llbracket \mathbf{u}_h \rrbracket\} \,\mathrm{d}\sigma, \tag{15}$$

where we simply applied definition (13). Moreover, introducing the symbol

$$\mathbf{r}(\llbracket \mathbf{u}_h \rrbracket) \overset{\text{def}}{=} \sum_{e \in \mathscr{E}_h} \mathbf{r}_e(\llbracket \mathbf{u}_h \rrbracket)$$

it is possible to show that one part of the consistency term in the discretization of the Laplacian acts indeed as a gradient correction. Summarizing the above remarks, we obtain the following equivalent form for Eq. (14): find $(\mathbf{u}_h, p_h) \in \mathbf{V}_h \times Q_h$ such that

$$\begin{aligned}
&\int_{\Omega_h} \mathbf{v}_h \cdot \frac{\partial \mathbf{u}_h}{\partial t}\,\mathrm{d}\mathbf{x} - \int_{\Omega_h} \nabla_h \mathbf{v}_h : (\mathbf{F}_v(\nabla_h \mathbf{u}_h, \mathbf{r}) + \mathbf{F}(\mathbf{u}_h, p_h))\,\mathrm{d}\mathbf{x} \\
&\quad + \int_{\Gamma_h} [\![\mathbf{v}_h]\!] : \left(\widehat{\mathbf{F}}_v(\nabla_h \mathbf{u}_h^+, \mathbf{r}_e^+; \nabla_h \mathbf{u}_h^-, \mathbf{r}_e^-) + \widehat{\mathbf{F}}(\mathbf{u}_h^+, p_h^+; \mathbf{u}_h^-, p_h^-) \right) \mathrm{d}\sigma = \int_{\Omega_h} \mathbf{v}_h \cdot \mathbf{g}\,\mathrm{d}\mathbf{x}, \\
&- \int_{\Omega_h} \nabla_h q_h \cdot \mathbf{u}_h\,\mathrm{d}\mathbf{x} + \int_{\Gamma_h} [\![q_h]\!] \cdot \hat{\mathbf{u}}(\mathbf{u}_h^+, p_h^+; \mathbf{u}_h^-, p_h^-)\,\mathrm{d}\sigma = 0
\end{aligned} \tag{16}$$

for all $(\mathbf{v}_h, q_h) \in \mathbf{V}_h \times Q_h$, where we introduced the viscous fluxes

$$\begin{aligned}
&\mathbf{F}_v(\nabla_h \mathbf{u}_h, \mathbf{r}) \stackrel{\text{def}}{=} -\nu(\nabla_h \mathbf{u}_h + \mathbf{r}([\![\mathbf{u}_h]\!])), \\
&\widehat{\mathbf{F}}_v(\nabla_h \mathbf{u}_h^+, \mathbf{r}_e^+; \nabla \mathbf{u}_h^-, \mathbf{r}_e^-) \stackrel{\text{def}}{=} -\nu(\{\nabla_h \mathbf{u}_h\} + \eta_e \{\mathbf{r}_e([\![\mathbf{u}_h]\!])\}).
\end{aligned}$$

3.1. Basis functions and numerical integration

According to Eq. (7), the test and trial functions are polynomials of degree k within each element $K \in \mathcal{T}_h$. Let $\bar{\mathbf{x}}^K \equiv (\bar{x}_1^K, \ldots, \bar{x}_N^K)$ be the coordinates of the centroid of a generic element $K \in \mathcal{T}_h$. The basis functions of the polynomial approximation of degree k associated with K are the scaled monomials

$$\varphi_i^K = \frac{\prod_{l=1}^N (x_l - \bar{x}_l^K)^{\alpha_{i,l}}}{\| \prod_{l=1}^N (x_l - \bar{x}_l^K)^{\alpha_{i,l}} \|_{0,K}}, \quad \sum_{l=1}^N \alpha_{i,l} \leqslant k, \tag{17}$$

where $\alpha_{i,1}, \ldots, \alpha_{i,N}$ are N nonnegative integers. The number of degrees of freedom for each component of $\mathbf{u}_h$ and for p_h within each element is given by

$$N_{\mathrm{DOF}}^K = \dim\{\varphi_i\} = \frac{\prod_{l=1}^N (k+l)}{N!}.$$

Having defined the basis functions in each element $K \in \mathcal{T}_h$, the polynomial approximation of $\mathbf{u}_h$ and p_h within K is given by

$$\mathbf{u}_h^K = \sum_{i=1}^{N_{\mathrm{DOF}}^K} \varphi_i^K \mathbf{U}_i^K, \qquad p_h^K = \sum_{i=1}^{N_{\mathrm{DOF}}^K} \varphi_i^K P_i^K, \tag{18}$$

where $\mathbf{U}_i^K$ and P_i^K are the degrees of freedom of the unknown velocity and pressure fields on $K \in \mathcal{T}_h$. The basis functions defined in Eq. (17) are also used to express the scalar and each component of the vector and tensor test functions.

All integrals appearing in Eq. (16) are computed by means of Gauss integration rules with a number of integration points suited for the required accuracy. Cheaper non-product formulae are preferred to tensor product ones when available. The quadrature formulae are taken from the encyclopædia of cubature formulae developed and maintained by Cools [13].

The numerical evaluation of volume and surface integrals in Eq. (16) requires to compute the basis functions at Gauss quadrature nodes. The coordinates $\mathbf{x}_G$ of each integration point in the physical frame are given by $\mathbf{x}_G = \mathbf{x}(\boldsymbol{\xi}_G)$, where $\boldsymbol{\xi}_G$ are the coordinates of Gauss quadrature nodes in the reference element and the functions $\mathbf{x}(\boldsymbol{\xi})$ define the (possibly nonlinear) mapping between the reference and the physical element. Notice that by defining the basis functions directly in the physical space one can obtain a polynomial form for the final algebraic expression of the integral of a polynomial function even if the mapping between the reference and the physical element is not linear.

3.2. Lifting operator

Let $e \subset \partial K^+ \cap \partial K^-$ be an internal face of the triangulation. According to its definition, the lifting operator applied to the jump of the velocity on e, $\mathbf{r}_e([\![\mathbf{u}_h]\!])$, is a second order tensor. Let us introduce the symbol $\mathbf{r}_{e,l}([\![\mathbf{u}_h]\!])$ to denote the vector corresponding to its lth column, i.e.

$$\mathbf{r}_{e,l}(\llbracket \mathbf{u}_h \rrbracket) \stackrel{\text{def}}{=} [(\mathbf{r}_e(\llbracket \mathbf{u}_h \rrbracket))_{i,l}]_{i=1,\ldots,N}.$$

We then have by Eq. (13) that $\mathbf{r}_e(\llbracket \mathbf{u}_h \rrbracket)$ is indeed the solution of the following problems:

$$\int_{\Omega_h} \mathbf{r}_{e,l}(\llbracket \mathbf{u}_h \rrbracket) \cdot \mathbf{v}_h \, \mathrm{d}\mathbf{x} = -\int_e \mathbf{l} \cdot \llbracket \mathbf{u}_h \rrbracket \cdot \{\mathbf{v}_h\} \, \mathrm{d}\sigma, \quad \forall \mathbf{v}_h \in \mathbf{V}_h, \;\; l = 1, \ldots, N, \tag{19}$$

$\mathbf{l}$ being the unit vector corresponding to the l-th space dimension. After some algebra it is possible to show that the above problem is indeed a local problem involving the mass matrices of the elements sharing e. Denoting with $\mathbf{R}^K_{e,l}$ the local vector of degrees of freedom associated to $\mathbf{r}_{e,l}(\llbracket \mathbf{u}_h \rrbracket)$ on element K, the local problem reads

$$\begin{bmatrix} \mathbf{M}^{K^+} & \mathbf{0} \\ \mathbf{0} & \mathbf{M}^{K^-} \end{bmatrix} \begin{bmatrix} \mathbf{R}^{K^+}_{e,l} \\ \mathbf{R}^{K^-}_{e,l} \end{bmatrix} = \underbrace{\begin{bmatrix} \mathbf{N}^{K^+,K^+}_{e,l} & \mathbf{N}^{K^+,K^-}_{e,l} \\ \mathbf{N}^{K^-,K^+}_{e,l} & \mathbf{N}^{K^-,K^-}_{e,l} \end{bmatrix}}_{\mathbf{N}_{e,l}} \begin{bmatrix} \mathbf{U}^{K^+} \\ \mathbf{U}^{K^-} \end{bmatrix}, \quad l = 1, \ldots, N,$$

where $\mathbf{M}^K$ indicates the local mass matrix on element K, $\mathbf{N}_{e,l}$ is the matrix corresponding to the bilinear form defined by the right-hand side of Eq. (19) and, according to the notation introduced in (18), the matrix–vector products have to be intended block-wise. From the above equation we immediately deduce that the following relation holds between the degrees of freedom of $\mathbf{r}_e(\llbracket \mathbf{u}_h \rrbracket)$ and those of the velocity on the elements sharing e:

$$\mathbf{R}^K_{e,l} = \sum_{H \in \{K^+, K^-\}} (\mathbf{M}^K)^{-1} \mathbf{N}^{K,H}_{e,l} \mathbf{U}^H, \quad K \in \{K^+, K^-\}, \;\; l = 1, \ldots, N.$$

The above fact is actually used in the computation of the lifting operator. The $\mathbf{N}^{K,H}_{e,l}$ as well as the elementary mass matrices are computed in a preliminary step and the products $(\mathbf{M}^K)^{-1}\mathbf{N}^{K,H}_{e,l}$ are stored at the beginning of the computation.

3.3. Boundary conditions and time discretization

The DG discretization is best suited for a weak enforcement of boundary conditions. For Dirichlet type boundary data, which is the case of the computations presented below, this can easily be achieved by properly defining a boundary state $\mathbf{u}^b_h$, p^b_h which, together with the internal state $\mathbf{u}^+_h$, p^+_h, allows to compute the numerical fluxes $\hat{\mathbf{u}}$, $\widehat{\mathbf{F}}$ and the function $\mathbf{r}^+_e$ on the portion Γ^∂_h of the boundary Γ_h. Moreover the averages $\{\nabla_h \mathbf{u}_h\}$ and $\{\mathbf{r}_e(\llbracket \mathbf{u}_h \rrbracket)\}$ in $\widehat{\mathbf{F}}_v$ are set equal to the internal values.

For the Stokes and Oseen problems computed in this paper the boundary state is simply set equal to the projection of the analytical solution onto the discrete space. This state takes the place of $\mathbf{u}^-_h$, p^-_h in the jump operators of Eq. (8) and in the numerical fluxes $\hat{\mathbf{u}}$ and $\widehat{\mathbf{F}}$ whilst in the lifting operator $\mathbf{r}^+_e$ the average of the test function is set equal to the internal value.

On the other hand, the wall-type boundary conditions of the lid-driven cavity flow have been implemented by defining the boundary state on the exterior of boundary faces as $\mathbf{u}^b_h = \mathbf{u}^-_h = -\mathbf{u}^+_h + 2\mathbf{z}_w$, $p^b_h = p^-_h = p^+_h$, where $\mathbf{z}_w$ is the velocity of a possibly sliding wall. In this case, therefore, the external boundary state exactly replaces $\mathbf{u}^-_h$ and p^-_h in the jump operators, in the numerical fluxes and in the lifting operator.

The discrete problem corresponding to Eq. (16) reads, in matrix form

$$\mathbf{M}\frac{\mathrm{d}\mathbf{W}}{\mathrm{d}t} + \mathbf{a}(\mathbf{W}) = \mathbf{b}(\mathbf{g}), \tag{20}$$

where $\mathbf{W}$ is the global vector of unknown degrees of freedom and $\mathbf{M}$ is the global block diagonal mass matrix. Lacking the time derivative of pressure in the governing equations, the blocks of $\mathbf{M}$ corresponding to the pressure degrees of freedom are identically zero. Eq. (20) defines a system of (nonlinear) ODEs which has been discretized by means of the implicit backward Euler scheme. By linearizing at time level n, we are led to solve the following linear problem at each time step:

$$\underbrace{\left[\frac{\mathbf{M}}{\Delta t}+\frac{\partial \mathbf{a}(\mathbf{W}^n)}{\partial \mathbf{W}}\right]}_{\mathbf{A}}(\mathbf{W}^{n+1}-\mathbf{W}^n)=-\mathbf{a}(\mathbf{W}^n)+\mathbf{b}(\mathbf{g}), \tag{21}$$

where $\partial \mathbf{a}(\mathbf{W}^n)/\partial \mathbf{W}$ is the Jacobian matrix of the DG space discretization and the symbol $\mathbf{A}$ denotes the linear system matrix. The matrix $\mathbf{A}$ can be regarded as an $N_K \times N_K$ block sparse matrix where N_K is the number of elements in $\mathscr{T}_h$ and the rank of each block is $N_{\mathrm{DOF}}^K \times (N+1)$. Thanks to the DG discretization here adopted the degrees of freedom of a generic element K are only coupled with those of the neighbouring elements and the number of nonzero blocks for each (block) row K of the matrix $\mathbf{A}$ is therefore equal to the number of elements surrounding the element K plus one.

The Jacobian matrix of the DG discretization has been computed analytically without any approximation and, using very large time steps, the method can therefore achieve quadratic convergence in the computation of steady state solutions (in the limit $\Delta t \to \infty$, Eq. (21) is in fact identical to one iteration of the Newton method applied to the steady form of Eq. (20)). Preliminary computations of unsteady INS flows using more accurate time discretization schemes have already shown the promising potentialities of the method. This topic will be the subject of a future work.

Finally, we mention that the linear system of Eq. (21) can be solved using either direct or iterative solvers. For all the computations presented below we have used the direct solver available in PETSc [14], the software upon which our DG code relies for the purpose of parallelization.

4. Numerical results

In this section, we provide thorough testing of the method applied to the Stokes, Oseen and Navier–Stokes equations. For the Stokes case, we used the analytical solution reported in [2]. For the Oseen and Navier–Stokes cases we used the Kovasznay and the lid-driven cavity flow problems. A short description of the test cases is given below.

4.1. Stokes problem

We consider the analytical solution to the Stokes system with $\mathbf{g}=\mathbf{0}$ given by

$$u(x,y) = -\exp(x)(y\cos y+\sin y),$$
$$v(x,y) = \exp(x) y \sin y,$$
$$p(x,y) = 2\exp(x)\sin y.$$

The computational domain was taken to be $(-1,1)^2$ and Dirichlet boundary conditions, computed from the analytical solution, were imposed on $\partial\Omega$.

4.2. Kovasznay problem

This analytical solution for the two-dimensional Navier–Stokes equations with $\mathbf{g}=\mathbf{0}$ was derived by Kovasznay in [8]. The analytical expression for the velocity and the pressure is

$$u(x,y) = 1-\exp(\lambda x)\cos(2\pi y),$$
$$v(x,y) = \frac{\lambda}{2\pi}\exp(\lambda x)\sin(2\pi y),$$
$$p(x,y) = -\frac{1}{2}\exp(2\lambda x)+C,$$

where the parameter λ depends on the Reynolds number Re according to the following relation:

$$\lambda = \frac{Re}{2}-\sqrt{\frac{Re^2}{4}+4\pi^2},$$

and C is an arbitrary constant. The same problem can be used as a benchmark for the Oseen equations provided we assume the advection field given by the analytical solution $\mathbf{u}$. The computational domain considered is

$$\Omega = \left(-\tfrac{1}{2}, \tfrac{3}{2}\right) \times (0, 2)$$

with prescribed Dirichlet boundary conditions on $\partial\Omega$.

4.3. Lid-driven cavity flow

The lid-driven cavity flow is one of the most extensively studied problems in fluid dynamics. It consists of solving the incompressible flow in the square cavity $(0,1)^2$ where homogeneous Dirichlet boundary conditions are imposed for the velocity except on the upper edge, where the velocity is $(1,0)$. Despite its simple geometry, the lid-driven cavity flow displays some features, which are challenging for any numerical method: the solution in the upper corners of the cavity is singular and, increasing the Reynolds number, the flow configuration rapidly changes and multiple counter rotating vortices with largely different sizes appear. The results are compared with those presented in [9–11].

4.4. Computational details

The cases for which an analytical solution is available were run on uniform $\mathbb{P}_k$ rectangular meshes of size $h = 2^{1-\sigma}$ with $\sigma = 4, \ldots, 9$, and hence from 8×8 to 256×256 elements. Also the lid-driven cavity flow was discretized with rectangular $\mathbb{P}_k$ elements, but the meshes were refined towards the boundaries. The maximum grid spacing $h_{\max} = 4.5 \times 10^{-2}$ was the same for the three Reynolds numbers considered, whilst the minimum grid spacing was reduced (and the grid size increased) as the Reynolds number was increased, i.e. $h_{\min} = 3.8 \times 10^{-3}$ (60×60 elements) at $Re = 1000$, $h_{\min} = 1.2 \times 10^{-3}$ (80×80 elements) at $Re = 10{,}000$, $h_{\min} = 8.5 \times 10^{-4}$ (88×88 elements) at $Re = 20{,}000$.

As regards the value of the artificial compressibility parameter c, we present the results of the Stokes problem for two fixed values of c, namely 1 and 0.1, chosen on the basis of numerical experiments, and for c varying as $1/h$ according to the analysis presented in [12, Chapter 4]. Since for the Oseen and Navier–Stokes case an analysis is not available yet, we have chosen to present the results for three values of the parameter c, 1, v/h and 0.1, in order to estimate the sensitivity of the method.

4.5. Comments

The velocity plots and the convergence results for the Stokes and Kovasznay problems are shown in Fig. 2 and in Tables 1–9. The monitored quantities are the L^2 errors of the velocity and pressure and the residual of

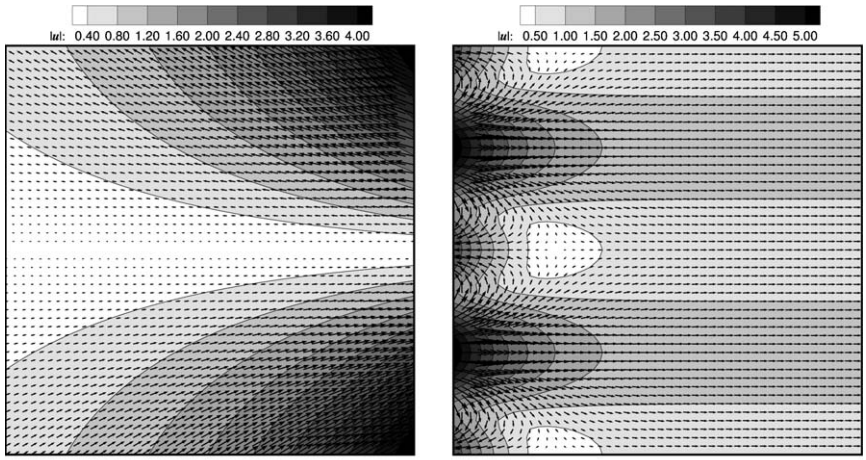

(a) Velocity plot of Stokes flow. (b) Velocity plot of Kovasznay flow.

Fig. 2. Results for the Stokes and Kovasznay problems.

Table 1
Convergence results for the Stokes equations with $\mathbb{P}_1$ elements

c	Grid size	$\|e_{\mathbf{u}}\|_0$		$\|e_p\|_0$		$\|e_{\nabla\cdot\mathbf{u}}\|_0$	
		Error	Order	Error	Order	Error	Order
1	32×32	1.01e−3	2.00	3.35e−3	1.46	1.44e−3	1.36
	64×64	2.53e−4	1.99	1.19e−3	1.49	5.63e−4	1.35
	128×128	6.38e−5	1.99	4.14e−4	1.53	2.13e−4	1.41
$1/h$	32×32	1.00e−3	2.00	7.87e−3	1.09	9.36e−4	1.44
	64×64	2.52e−4	1.99	3.76e−3	1.07	3.65e−4	1.36
	128×128	6.36e−5	1.99	1.82e−3	1.04	1.39e−4	1.39
10^{-1}	32×32	1.01e−3	2.01	2.91e−3	1.47	1.71e−3	1.40
	64×64	2.54e−4	1.99	9.85e−4	1.56	6.62e−4	1.37
	128×128	6.39e−5	1.99	3.40e−4	1.53	2.44e−4	1.44

Table 2
Convergence results for the Stokes equations with $\mathbb{P}_2$ elements

c	Grid size	$\|e_{\mathbf{u}}\|_0$		$\|e_p\|_0$		$\|e_{\nabla\cdot\mathbf{u}}\|_0$	
		Error	Order	Error	Order	Error	Order
1	16×16	9.36e−5	3.01	2.87e−4	2.16	9.66e−4	1.99
	32×32	1.16e−5	3.01	7.55e−5	1.93	2.44e−4	1.98
	64×64	1.45e−6	3.00	2.05e−5	1.88	6.17e−5	1.98
$1/h$	16×16	9.33e−5	3.01	4.34e−4	1.91	9.63e−4	1.95
	32×32	1.16e−5	3.01	1.25e−4	1.79	2.48e−4	1.96
	64×64	1.45e−6	3.00	3.41e−5	1.88	6.29e−5	1.98
10^{-1}	16×16	9.48e−5	3.02	2.92e−4	2.35	9.78e−4	2.05
	32×32	1.17e−5	3.01	6.62e−5	2.14	2.42e−4	2.02
	64×64	1.46e−6	3.01	1.63e−5	2.02	6.03e−5	2.00

Table 3
Convergence results for the Stokes equations with $\mathbb{P}_3$ elements

c	Grid size	$\|e_{\mathbf{u}}\|_0$		$\|e_p\|_0$		$\|e_{\nabla\cdot\mathbf{u}}\|_0$	
		Error	Order	Error	Order	Error	Order
1	8×8	2.87e−5	4.00	1.54e−4	2.84	3.08e−4	2.96
	16×16	1.78e−6	4.01	2.10e−5	2.88	3.93e−5	2.97
	32×32	1.10e−7	4.01	2.82e−6	2.90	5.02e−6	2.97
$1/h$	8×8	2.86e−5	4.00	1.89e−4	2.74	3.04e−4	2.93
	16×16	1.76e−6	4.01	2.67e−5	2.82	3.98e−5	2.93
	32×32	1.10e−7	4.01	3.60e−6	2.89	5.12e−6	2.96
10^{-1}	8×8	2.89e−5	4.00	1.18e−4	2.97	2.99e−4	3.05
	16×16	1.79e−6	4.02	1.56e−5	2.91	3.65e−5	3.03
	32×32	1.11e−7	4.01	2.12e−6	2.88	4.56e−6	3.00

the incompressibility constraint, denoted as $\|e_{\nabla\cdot\mathbf{u}}\|_0$. All the errors were normalized with respect to the domain measure.

In the Stokes case the results for $c = 1/h$ are like those reported in [2] and it is shown in [12] that this is consistent with the theoretical comparison of the method here proposed with that introduced in [2]. An interesting remark is that, when c is taken of order 1, superconvergence is observed for the pressure, whose error apparently scales with order equal to $k + 1/2$ for $\mathbb{P}_1$ elements.

Table 4
Convergence results for the Oseen equations with $\mathbb{P}_1$ elements

c	Grid size	$\|e_{\mathbf{u}}\|_0$		$\|e_p\|_0$		$\|e_{\nabla\cdot\mathbf{u}}\|_0$	
		Error	Order	Error	Order	Error	Order
1	32×32	1.03e−2	2.09	2.03e−2	1.81	6.68e−2	1.90
	64×64	2.47e−3	2.06	5.30e−3	1.94	1.63e−2	2.03
	128×128	6.10e−4	2.02	1.31e−3	2.01	4.10e−3	2.00
	256×256	1.53e−4	2.00	3.25e−4	2.01	1.14e−3	1.84
ν/h	32×32	1.03e−2	2.16	2.03e−2	1.81	6.68e−2	1.95
	64×64	2.43e−3	2.06	5.78e−3	1.83	1.46e−2	2.11
	128×128	6.02e−4	2.01	1.89e−3	1.61	3.56e−3	2.04
	256×256	1.51e−4	1.99	7.90e−4	1.26	9.48e−4	1.91
10^{-1}	32×32	1.05e−2	2.18	1.95e−2	1.88	7.26e−2	2.01
	64×64	2.48e−3	2.08	5.04e−3	1.95	1.72e−2	2.08
	128×128	6.11e−4	2.02	1.22e−3	2.04	4.21e−3	2.03
	256×256	1.53e−4	2.00	2.97e−4	2.04	1.16e−3	1.86

Table 5
Convergence results for the Oseen equations with $\mathbb{P}_2$ elements

c	Grid size	$\|e_{\mathbf{u}}\|_0$		$\|e_p\|_0$		$\|e_{\nabla\cdot\mathbf{u}}\|_0$	
		Error	Order	Error	Order	Error	Order
1	16×16	3.54e−3	3.01	8.12e−3	2.40	4.15e−2	2.24
	32×32	4.31e−4	3.04	1.33e−3	2.61	9.23e−3	2.17
	64×64	5.27e−5	3.03	2.18e−4	2.61	2.20e−3	2.07
	128×128	6.53e−6	3.01	3.98e−5	2.48	5.47e−4	2.01
ν/h	16×16	3.56e−3	3.05	8.16e−3	2.45	4.21e−2	2.35
	32×32	4.30e−4	3.05	1.33e−3	2.61	9.16e−3	2.20
	64×64	5.26e−5	3.03	2.28e−4	2.55	2.20e−3	2.06
	128×128	6.52e−6	3.01	4.44e−5	2.36	5.49e−4	2.01
10^{-1}	16×16	3.61e−3	3.06	8.15e−3	2.49	4.38e−2	2.36
	32×32	4.33e−4	3.06	1.31e−3	2.64	9.31e−3	2.23
	64×64	5.28e−5	3.04	2.08e−4	2.65	2.19e−3	2.09
	128×128	6.52e−6	3.02	3.64e−5	2.51	5.42e−4	2.01

Table 6
Convergence results for the Oseen equations with $\mathbb{P}_3$ elements

c	Grid size	$\|e_{\mathbf{u}}\|_0$		$\|e_p\|_0$		$\|e_{\nabla\cdot\mathbf{u}}\|_0$	
		Error	Order	Error	Order	Error	Order
1	8×8	3.98e−3	3.73	6.93e−3	3.18	3.56e−2	2.90
	16×16	2.53e−4	3.94	6.72e−4	3.37	4.83e−3	2.88
	32×32	1.59e−5	4.00	6.42e−5	3.39	6.40e−4	2.92
	64×64	9.88e−7	4.01	6.88e−6	3.22	8.23e−5	2.96
ν/h	8×8	3.90e−3	3.74	6.66e−3	3.19	3.75e−2	2.97
	16×16	2.53e−4	3.94	6.67e−4	3.32	4.87e−3	2.95
	32×32	1.59e−5	4.00	6.60e−5	3.38	6.36e−4	2.94
	64×64	9.87e−7	4.01	7.43e−6	3.15	8.17e−5	2.96
10^{-1}	8×8	3.92e−3	3.73	6.62e−3	3.18	3.86e−2	2.96
	16×16	2.55e−4	3.94	6.75e−4	3.29	4.94e−3	2.96
	32×32	1.59e−5	4.00	6.31e−5	3.42	6.38e−4	2.95
	64×64	9.89e−7	4.01	6.65e−6	3.25	8.12e−5	2.97

Table 7
Convergence results for the Navier–Stokes equations with $\mathbb{P}_1$ elements

c	Grid size	$\|e_{\mathbf{u}}\|_0$		$\|e_p\|_0$		$\|e_{\nabla\cdot\mathbf{u}}\|_0$	
		Error	Order	Error	Order	Error	Order
1	32×32	9.95e−3	2.06	1.81e−2	1.88	6.33e−2	1.82
	64×64	2.43e−3	2.03	4.74e−3	1.93	1.61e−2	1.98
	128×128	6.08e−4	2.00	1.20e−3	1.98	4.10e−3	1.97
	256×256	1.52e−4	1.99	3.11e−4	1.95	1.14e−3	1.84
v/h	32×32	9.86e−3	2.09	1.86e−2	1.84	6.04e−2	1.92
	64×64	2.40e−3	2.04	5.40e−3	1.78	1.46e−2	2.05
	128×128	6.01e−4	2.00	1.84e−3	1.55	3.62e−3	2.01
	256×256	1.52e−4	1.99	7.86e−4	1.23	9.72e−4	1.90
10^{-1}	32×32	1.01e−2	2.13	1.73e−2	1.99	6.77e−2	1.89
	64×64	2.45e−3	2.04	4.51e−3	1.94	1.68e−2	2.01
	128×128	6.09e−4	2.01	1.13e−3	2.00	4.20e−3	2.00
	256×256	1.53e−4	1.99	2.90e−4	1.96	1.16e−3	1.86

Table 8
Convergence results for the Navier–Stokes equations with $\mathbb{P}_2$ elements

c	Grid size	$\|e_{\mathbf{u}}\|_0$		$\|e_p\|_0$		$\|e_{\nabla\cdot\mathbf{u}}\|_0$	
		Error	Order	Error	Order	Error	Order
1	16×16	3.52e−3	3.05	7.30e−3	2.49	4.08e−2	2.28
	32×32	4.29e−4	3.04	1.21e−3	2.59	9.13e−3	2.16
	64×64	5.26e−5	3.03	2.04e−4	2.56	2.20e−3	2.06
	128×128	6.52e−6	3.01	3.78e−5	2.44	5.47e−4	2.01
v/h	16×16	3.52e−3	3.09	7.3e−3	2.54	4.12e−2	2.35
	32×32	4.28e−4	3.04	1.22e−3	2.58	9.08e−3	2.18
	64×64	5.25e−5	3.03	2.16e−4	2.50	2.20e−3	2.05
	128×128	6.51e−6	3.01	4.32e−5	2.32	5.49e−4	2.00
10^{-1}	16×16	3.55e−3	3.11	7.15e−3	2.59	4.24e−2	2.36
	32×32	4.30e−4	3.04	1.18e−3	2.60	9.20e−3	2.20
	64×64	5.26e−5	3.03	1.96e−4	2.60	2.19e−3	2.07
	128×128	6.52e−6	3.01	3.58e−5	2.45	5.44e−4	2.01

Table 9
Convergence results for the Navier–Stokes equations with $\mathbb{P}_3$ elements

c	Grid size	$\|e_{\mathbf{u}}\|_0$		$\|e_p\|_0$		$\|e_{\nabla\cdot\mathbf{u}}\|_0$	
		Error	Order	Error	Order	Error	Order
1	8×8	3.92e−3	3.75	7.46e−3	3.43	3.52e−2	2.95
	16×16	2.54e−4	3.95	6.98e−4	3.42	4.82e−3	3.08
	32×32	1.59e−5	4.00	6.66e−5	3.39	6.42e−4	2.91
	64×64	9.88e−7	4.01	7.09e−6	3.23	8.27e−5	2.96
v/h	8×8	3.93e−3	3.76	7.23e−3	3.42	3.65e−2	3.02
	16×16	2.54e−4	3.95	6.95e−4	3.38	4.84e−3	2.92
	32×32	1.59e−5	4.00	6.79e−5	3.35	6.38e−4	2.92
	64×64	9.87e−7	4.01	7.54e−6	3.17	8.19e−5	2.96
10^{-1}	8×8	3.92e−3	3.76	7.12e−3	3.42	3.72e−2	3.02
	16×16	2.55e−4	3.94	7.03e−4	3.34	4.90e−3	2.93
	32×32	1.59e−5	4.00	6.59e−5	3.41	6.45e−4	2.93
	64×64	9.89e−7	4.01	6.98e−6	3.24	8.24e−5	2.97

The Oseen case cannot be traced back to the method presented in [3] due to the different handling of the convective term. Tables 4–6 show that, as it could be expected, the velocity converges with order $k+1$, while superconvergence is again observed for the pressure, which converges with order $k+1$ in the $\mathbb{P}_1$ case and with order between k and $k+1/2$ in the $\mathbb{P}_2$ and $\mathbb{P}_3$ cases, for $c = \mathcal{O}(1)$. Both here and in the Stokes case, the scaling of the incompressibility parameter c with the mesh size seems to be harmful with respect to the potentiality of the method.

Similar considerations hold true for the results obtained in the Navier–Stokes case, where again the pressure appears to converge with order 2 in the $\mathbb{P}_1$ case and with order between k and $k+1/2$ when $k \geqslant 2$. When comparing these results with those presented in [4], we notice not only that our method achieves a higher order of convergence for the pressure, but also that the absolute errors are significantly smaller, suggesting smaller values for the constants in the convergence estimates with respect to those in [4]. The analysis of the superconvergence results will be the subject of a future work.

For both linear problems we also evaluated the condition number $K_{\mathbf{A}}$ of the matrix $\mathbf{A}$ in Eq. (21) for $\Delta t \to \infty$, i.e. the condition number of the Jacobian matrix derived from the DG space discretization. It is quite

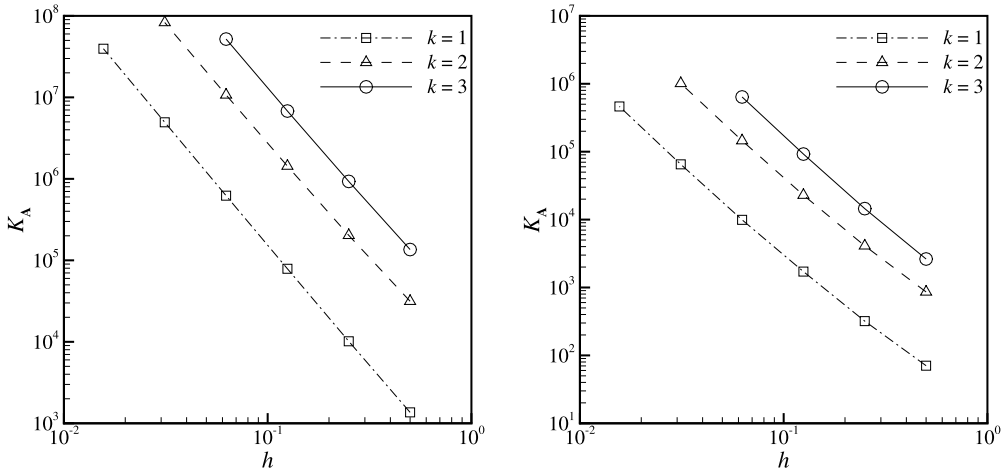

(a) Stokes problem. (b) Kovasznay problem.

Fig. 3. Matrix condition number for the Stokes and Oseen equations ($c = 1$).

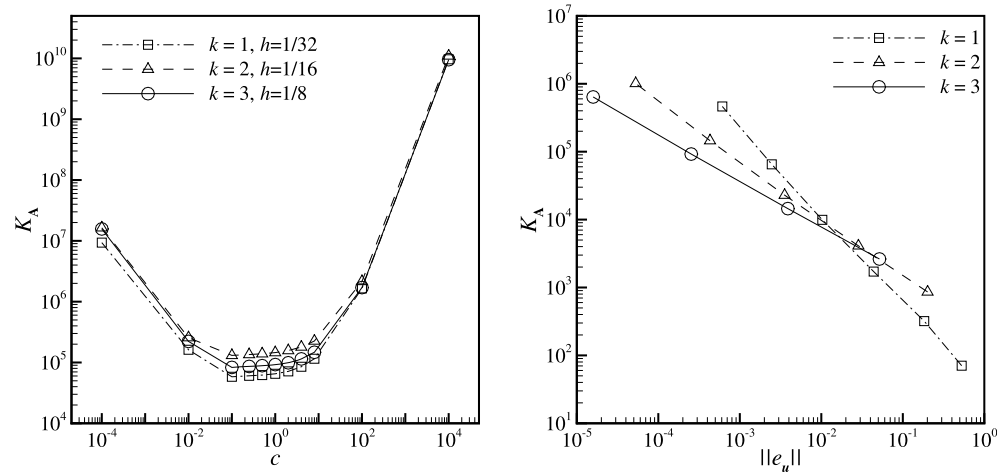

(a) Effect of artificial compressibility. (b) Dependence on velocity error.

Fig. 4. Matrix condition number for the Oseen equations.

easy to observe in Figs. 3(a) and (b) that, decreasing the grid size, the growing rate of K_A is not dependent on the degree of the polynomial approximation and is equal to 3, i.e. halving the mesh size the condition number becomes eight times bigger. Two more results of the numerical experiments with the Oseen equations concern the behaviour of K_A as a function of the artificial compressibility parameter c and of the error of the numerical solution, for different degrees of polynomial approximation and grid sizes. Fig. 4(a) shows that there is a broad range of values of c, around $c = 1$ and not dependent on k, for which K_A is slowly changing, whereas a rapid growth is observed outside this range. Fig. 4(b) indicates that in the region of small errors on the velocity, i.e. the left part of the graphic, we obtain better condition numbers with the higher order approximations. Similar results hold for the pressure.

As regards the lid-driven cavity flow, the results of the computations are summarized in Figs. 5–7. For the three Reynolds numbers considered our method proved able to mimic the available results with great accuracy. The method proved highly stable and a steady solution was found even for the highest Reynolds number case, i.e. $Re = 20{,}000$. The physical relevance of this result, however, should be considered with some caution

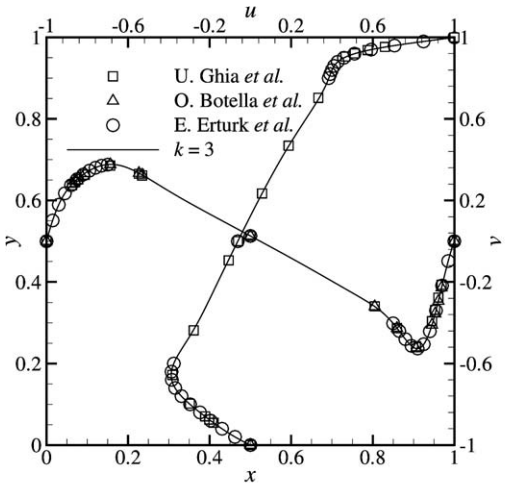

(a) u- and v-velocity on vertical and horizontal centerlines.

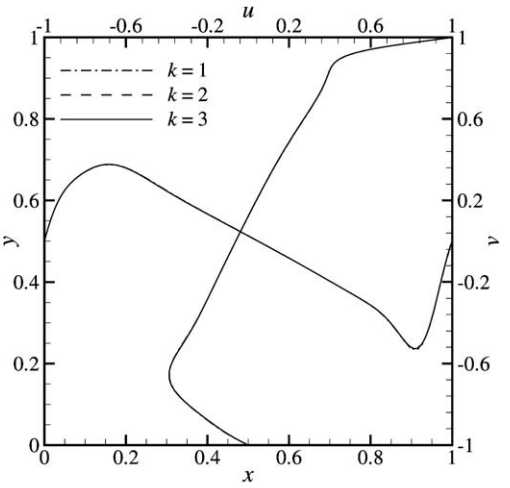

(b) u- and v-velocity on vertical and horizontal centerlines: $\mathbb{P}_1$, $\mathbb{P}_2$ and $\mathbb{P}_3$ solutions.

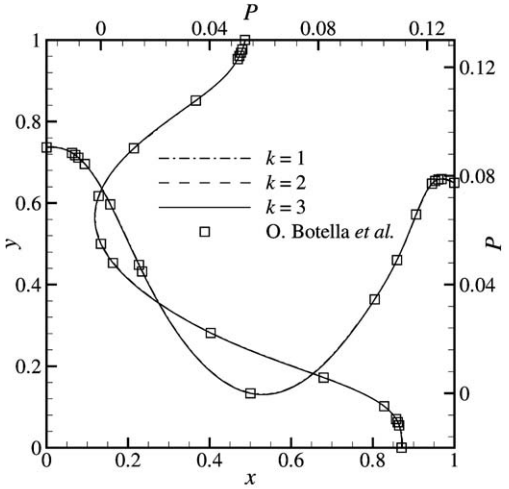

(c) Pressure on vertical and horizontal centerlines.

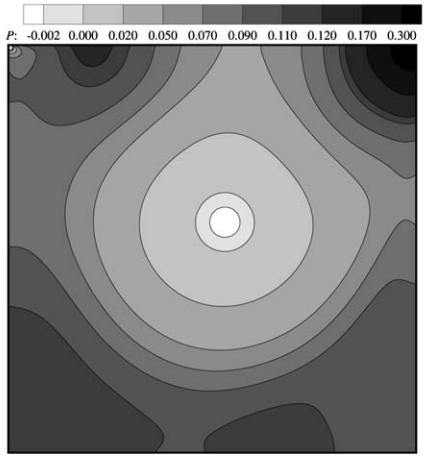

(d) Pressure plot of $\mathbb{P}_3$ solution.

Fig. 5. Results for the lid-driven cavity flow ($Re = 1000$).

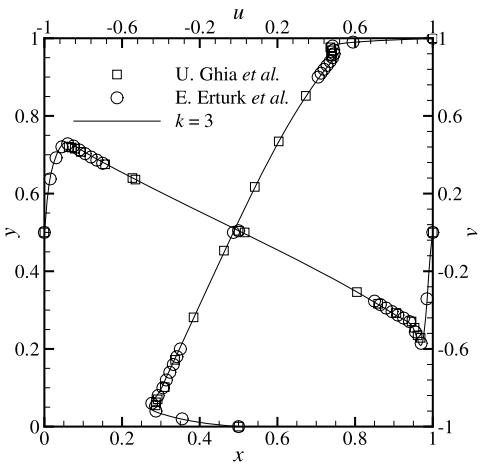

(a) u- and v-velocity on vertical and horizontal centerlines.

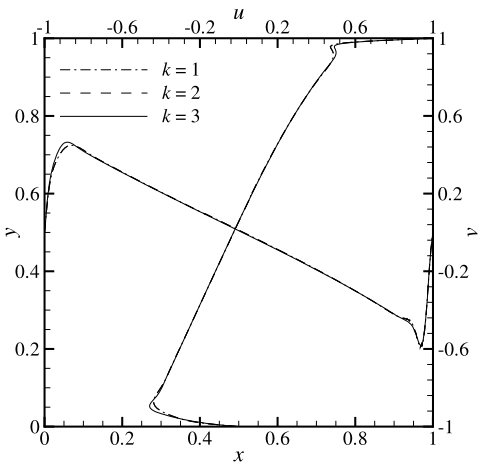

(b) u- and v-velocity on vertical and horizontal centerlines: P_1, P_2 and P_3 solutions.

Fig. 6. Results for the lid-driven cavity flow ($Re = 10{,}000$).

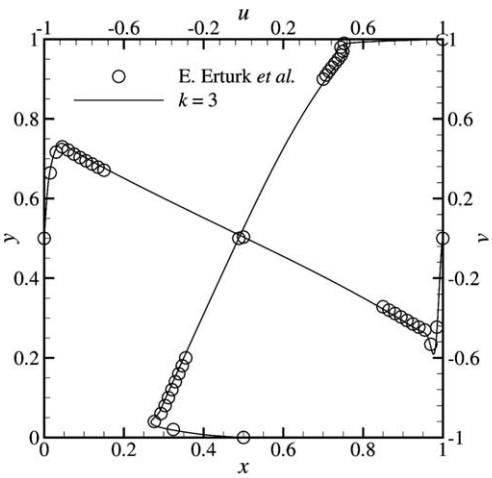

(a) u- and v-velocity on vertical and horizontal centerlines.

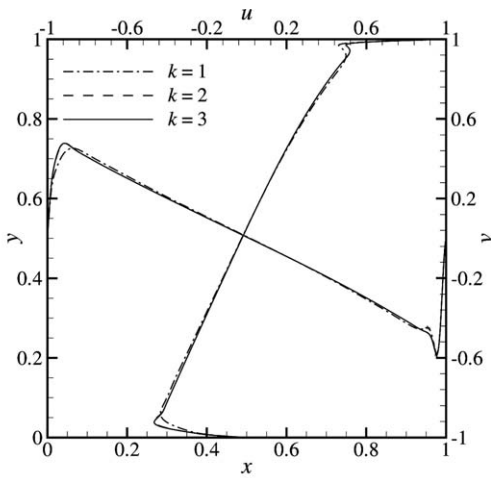

(b) u- and v-velocity on vertical and horizontal centerlines: $\mathbb{P}_1$, $\mathbb{P}_2$ and $\mathbb{P}_3$ solutions.

(c) Velocity plot of $\mathbb{P}_3$ solution.

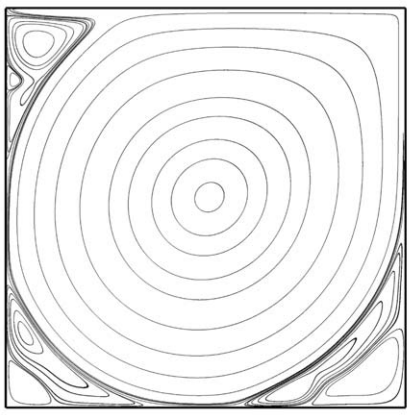

(d) Streamlines plot of $\mathbb{P}_3$ solution.

Fig. 7. Results for the lid-driven cavity flow ($Re = 20{,}000$).

because the strong damping properties of the backward Euler scheme could have altered the physics of the flow by suppressing physical instabilities.

We close this section with a final comment on the boundary condition for pressure in the lid-driven cavity flow. For this problem, in fact, the wall boundary condition for pressure outlined in Section 3.3 leaves the pressure field defined up to an additive constant. From a numerical point of view the consequence is that the problem matrix has rank one unit less than the number of unknowns. The problem can be solved in the customary way by eliminating one degree of freedom. In continuous finite elements approximations, however, this may give rise to a bad behaviour of the solution in the neighborhood of the deleted node when no special care is paid. Such a phenomenon is not observed in the DG approximation proposed in this work.

5. Conclusions

In this work we presented an artificial compressibility numerical flux for the DG approximation of the incompressible Navier–Stokes equations. The key idea is to add an artificial compressibility-like perturbation for the sole purpose of inter-element flux computation, thus recovering a hyperbolic problem. With respect to other methods presented in the literature, this requires the solution of a nonlinear equation in order to obtain the values of the unknowns to be used in flux evaluation, which, however, does not entail a sensible variation of computational cost. Although originally thought for the Navier–Stokes equations, the method can be easily applied to the Stokes and Oseen cases.

Numerical validation was provided by testing the method against a number of well-known benchmark problems. In all cases, the method exhibited superconvergence for the pressure for the artificial compressibility parameter of order 1. Improvement in terms of accuracy seems also to be present with respect to other methods. The theoretical investigation of these results is the subject of ongoing work.

Appendix A. Riemann solvers

In this section we describe the exact Riemann solver for the computation of the inviscid numerical fluxes $\widehat{\mathbf{F}}(\cdot,\cdot;\cdot,\cdot)$ and $\hat{\mathbf{u}}(\cdot,\cdot;\cdot,\cdot)$ in the Navier–Stokes, Oseen and Stokes cases. We refer interested readers to [15] for previous work on Riemann solvers with artificial compressibility for the incompressible Navier–Stokes equations.

A.1. Riemann solver for the Navier–Stokes equations

With reference to Eq. (11), in the Navier–Stokes case we have to solve the Riemann problem for the nonlinear system

$$\frac{\partial \mathbf{w}}{\partial t} + \frac{\partial \mathbf{F}(\mathbf{w})}{\partial x} = \mathbf{0}, \tag{A.1}$$

with initial datum

$$\mathbf{w} = \begin{cases} \mathbf{w}_L & \text{if } x < 0, \\ \mathbf{w}_R & \text{if } x > 0, \end{cases}$$

where the unknown $\mathbf{w}$ and the flux $\mathbf{F}(\mathbf{w})$ are given by

$$\mathbf{w} = \begin{bmatrix} p \\ u \\ \mathbf{v} \end{bmatrix}, \qquad \mathbf{F}(\mathbf{w}) = \begin{bmatrix} c^2 u \\ u^2 + p \\ u\mathbf{v} \end{bmatrix}, \tag{A.2}$$

being $\mathbf{v}$ the tangential component of the velocity (a scalar in 2D, a vector in 3D). In the sequel we give a detailed exposition for the 2D case and point out a simple way to generalize the results to the 3D case. The Jacobian matrix $\mathbf{A} = \partial\mathbf{F}(\mathbf{w})/\partial\mathbf{w}$ and the left and the right eigenvectors matrices $\mathbf{L}$ and $\mathbf{R}$ are given by

$$\mathbf{A} = \begin{bmatrix} 0 & c^2 & 0 \\ 1 & 2u & 0 \\ 0 & v & u \end{bmatrix}, \qquad \mathbf{L} = \begin{bmatrix} 1 & u-a & 0 \\ 1 & u+a & 0 \\ 1 & u & -\dfrac{a^2}{v} \end{bmatrix}, \qquad \mathbf{R} = \frac{1}{2a}\begin{bmatrix} u+a & -u+a & 0 \\ -1 & 1 & 0 \\ \dfrac{v}{a} & \dfrac{v}{a} & -\dfrac{2v}{a} \end{bmatrix}, \tag{A.3}$$

and the eigenvalues of **A** are

$$\lambda_- = u - a, \qquad \lambda_+ = u + a, \qquad \lambda_0 = u, \tag{A.4}$$

where

$$a = \sqrt{u^2 + c^2} \tag{A.5}$$

plays the same role as the speed of sound in the compressible Euler equations. By the definition of a it is readily seen that $\lambda_- < 0$ and $\lambda_+ > 0$.

The solution of the Riemann problem entails four states separated by two centered waves, hereafter called "left" and "right" waves, and by a contact discontinuity, across which the sole tangential velocity component can vary. The left and right waves can be either shocks or centered isentropic rarefactions, depending on the initial data. As shown in Fig. A.1, the star denotes the region of the solution holding on the $x/t = 0$ line. After characterizing the Riemann invariants and writing the Rankine–Hugoniot jump conditions, in Section A.1.3 we will describe how to find the state u_*, p_* in the star region for all possible cases of left and right waves, while in Section A.1.4 we will describe the procedure to obtain $\mathbf{v}_*$, the tangential velocity component on the $x/t = 0$ line.

A.1.1. Riemann invariants

We first characterize the Riemann invariants $\Gamma_{\pm,0}(p,u,v)$ of problem (A.1). By definition, the gradients of the Riemann invariants are the left eigenvectors of **A**, i.e. the rows of **L** (see Eq. A.3). The Riemann invariants $\Gamma_{\pm,0}$ assume constant values along the "characteristic curves" $C_{\pm,0}$ of equation $x_{\pm,0}(t)$ and slope $\mathrm{d}x_{\pm,0}(t)/\mathrm{d}t = \lambda_{\pm,0}$, i.e.

$$\mathrm{d}\Gamma_{\pm,0} = 0 \quad \text{along } x_{\pm,0}(t), \ \frac{\mathrm{d}x}{\mathrm{d}t} = \lambda_{\pm,0}.$$

We therefore obtain

$$\mathrm{d}\Gamma_- = \mathrm{d}p + (u-a)\,\mathrm{d}u = 0 \quad \text{on } C_-, \tag{A.6a}$$

$$\mathrm{d}\Gamma_+ = \mathrm{d}p + (u+a)\,\mathrm{d}u = 0 \quad \text{on } C_+, \tag{A.6b}$$

$$\mathrm{d}\Gamma_0 = \mathrm{d}p + u\,\mathrm{d}u - a^2\frac{\mathrm{d}v}{v} = 0 \quad \text{on } C_0. \tag{A.6c}$$

The first two relations can be integrated to get

$$\begin{aligned} \Gamma_- &= p + \frac{1}{2}[u(u-a) - c^2\log(u+a)] = \Gamma_-^0 \quad \text{on } C_-, \\ \Gamma_+ &= p + \frac{1}{2}[u(u+a) + c^2\log(u+a)] = \Gamma_+^0 \quad \text{on } C_+, \end{aligned} \tag{A.7}$$

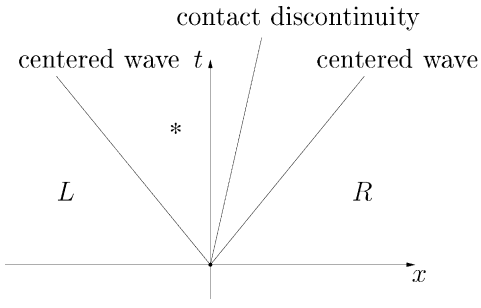

Fig. A.1. Structure of the Riemann problem.

where $\Gamma_{\pm}^{0}$ are constant values. Notice that in a left (resp. in a right) rarafection wave, the Riemann invariant Γ_{+} (resp. Γ_{-}) is constant since a left rarefaction is crossed by C_{+} lines and a right rarefaction by C_{-} lines. The third Riemann invariant Γ_{0} will be exploited in the computation of the tangential velocity component in Section A.1.4.

A.1.2. Rankine–Hugoniot jump conditions

The jumps $\mathbf{w}_2 - \mathbf{w}_1$ and $\mathbf{F}_2 - \mathbf{F}_1$ across a shock are related to each other by the Rankine–Hugoniot relations

$$\mathbf{F}(\mathbf{w}_2) - \mathbf{F}(\mathbf{w}_1) = s(\mathbf{w}_2 - \mathbf{w}_1),$$

where s denotes the shock speed. We therefore have

$$c^2(u_2 - u_1) = s(p_2 - p_1), \tag{A.8a}$$

$$\left(u_2^2 + p_2 - u_1^2 - p_1\right) = s(u_2 - u_1), \tag{A.8b}$$

$$(u_2 v_2 - u_1 v_1) = s(v_2 - v_1). \tag{A.8c}$$

It is an easy matter to eliminate the jump $(p_2 - p_1)$ from Eqs. (A.8a) and (A.8b) so as to obtain the shock speed s as a function of u_1 and u_2, i.e.

$$s_{\pm} = \frac{u_1 + u_2}{2} \pm \sqrt{\left(\frac{u_1 + u_2}{2}\right)^2 + c^2}. \tag{A.9}$$

Notice that $s_{-} < 0$ and that $s_{+} > 0$. The pressure jump $(p_2 - p_1)$ and the tangential velocity ratio v_2/v_1 are then given by

$$p_2 - p_1 = \frac{c^2(u_2 - u_1)}{s_{\pm}}, \tag{A.10}$$

$$\frac{v_2}{v_1} = \frac{u_1 - s_{\pm}}{u_2 - s_{\pm}}. \tag{A.11}$$

A.1.3. Pressure and normal velocity component

The pressure and the normal component of the velocity in the star region can be obtained as a function of $\mathbf{w}_L$ and $\mathbf{w}_R$ by exploiting the preservation of the Riemann invariants across the isentropic rarefactions and the Rankine–Hugoniot jump conditions across the shocks. Since the pressure always appears linearly in Eq. (A.7) as well as in Eq. (A.10), it is as easy matter to obtain the pressure jumps in the four possible cases.

- If the left wave is a rarefaction then the Γ_{+} Riemann invariant is conserved and

$$p_L + \frac{1}{2}\left[u_L(u_L + a_L) + c^2 \log(u_L + a_L)\right] = p_* + \frac{1}{2}\left[u_*(u_* + a_*) + c^2 \log(u_* + a_*)\right],$$

that is

$$p_L - p_* - f_{LW}^{R}(u_L, u_*) = 0, \tag{A.12}$$

with

$$f_{LW}^{R}(u_L, u_*) \stackrel{\text{def}}{=} \frac{1}{2}\left[u_*(u_* + a_*) + c^2 \log(u_* + a_*) - u_L(u_L + a_L) - c^2 \log(u_L + a_L)\right].$$

- If the left wave is a shock we exploit the Rankine–Hugoniot jump condition (A.10) to obtain

$$p_L - p_* - f_{LW}^{S}(u_L, u_*) = 0, \tag{A.13}$$

with

$$f_{LW}^{S}(u_L, u_*) \stackrel{\text{def}}{=} \frac{c^2(u_L - u_*)}{s_{-}}.$$

- If the right wave is a rarefaction then the Γ_{-} Riemann invariant is conserved and

$$p_* - p_R + f_{RW}^{R}(u_*, u_R) = 0, \tag{A.14}$$

with

$$f_{RW}^{R}(u_*, u_R) \stackrel{\text{def}}{=} \frac{1}{2}\left[u_*(u_* - a_*) - c^2 \log(u_* + a_*) - u_R(u_R - a_R) + c^2 \log(u_R + a_R)\right].$$

- If the right wave is a shock equation (A.10) implies

$$p_* - p_R + f_{RW}^{S}(u_*, u_R) = 0, \tag{A.15}$$

with

$$f_{RW}^{S}(u_*, u_R) \stackrel{\text{def}}{=} \frac{c^2(u_R - u_*)}{s_+}.$$

To solve the problem in the star region we now have two equations in the unknowns u_* and p_* to be chosen among the four we derived above according to the nature of the left and right waves. The pressure p_* can be eliminated from Eqs. (A.12)–(A.15), thus obtaining an equation in u_* of the form

$$F(u_*) = p_L - p_R - f_{LW}^{X_i}(u_L, u_*) + f_{RW}^{X_i}(u_*, u_R) = 0, \tag{A.16}$$

with $X_i \in \{S, R\}, i = 1, 2$ depending on the nature of the centered waves, which can be decided by considering the entropy condition.

In order for the entropy condition to be satisfied, characteristics must converge into a shock, which implies the inequalities

$$\begin{aligned} (\lambda_-)_L > s_- > (\lambda_-)_* \quad &\Rightarrow \quad u_L - a_L > u_* - a_* \quad \Rightarrow \quad u_* < u_L, \\ (\lambda_+)_* > s_+ > (\lambda_+)_R \quad &\Rightarrow \quad u_* + a_* > u_R + a_R \quad \Rightarrow \quad u_* > u_R. \end{aligned} \tag{A.17}$$

Since, by inspection of Eqs. (A.9) and (A.10), for a left shock the sign of $[p]$ is different from that of $[u]$ while, for a right shock, the sign of $[p]$ is the same of that of $[u]$, we have that

$$u_* < u_L \quad \Rightarrow \quad p_* > p_L, \qquad u_* > u_R \quad \Rightarrow \quad p_* > p_R, \tag{A.18}$$

i.e. the entropy satisfying shocks are always compressive.

The value of the velocity component u_* in the star region can be obtained by solving the nonlinear Eq. (A.16) by the Newton method. At each iteration the correct wave pattern is selected by considering Eq. (A.17). The pressure can then be computed by using one of the equations we combined to get the equation for u_*. A relative convergence tolerance of 10^{-14} on pressure is typically achieved in 4 or 5 iterations.

A.1.4. Tangential velocity component

The tangential velocity component v_* can be obtained by integrating Eq. (A.6c) across the left or right centered waves depending on the sign of u_*.

- If $u_* > 0$ and the left wave is a rarefaction we exploit the fact that the Γ_+ Riemann invariant is preserved to write

$$\mathrm{d}p = -(u + a)\,\mathrm{d}u.$$

Substituting in Eq. (A.6c) we find

$$\frac{\mathrm{d}v}{v} + \frac{\mathrm{d}u}{a} = 0,$$

which, on integration between the left and star states, gives

$$\ln\frac{v_*}{v_L} + \ln\frac{u_* + a_*}{u_L + a_L} = 0,$$

or

$$\frac{v_*}{v_L} = \frac{u_L + a_L}{u_* + a_*}.$$

- If $u_* > 0$ and the left centered wave is a shock we apply Eq. (A.11) to the left and star states to obtain
$$\frac{v_*}{v_L} = \frac{u_L - s_-}{u_* - s_-}.$$
- If $u_* < 0$ and the wave facing to the right is a rarefaction then the Γ_- Riemann invariant is preserved. Integrating between the star and the right states we find
$$\frac{v_*}{v_R} = \frac{u_* + a_*}{u_R + a_R}.$$
- If $u_* < 0$ and the right centered wave is a shock equation (A.11) applied to the star and right states implies
$$\frac{v_*}{v_R} = \frac{u_R - s_+}{u_* - s_+}.$$

A.1.5. Generalization to the 3D case

The results above can be generalized to the three-dimensional case by observing that the additional equation introduced by the third component of the velocity has exactly the same form as the one for the second component. It is therefore not difficult to realize that the results collected in Table A.1 hold true.

A.2. Riemann solver for the Stokes and Oseen equations

In the homogeneous Stokes case we have to solve the system

$$\frac{\partial \mathbf{u}}{\partial t} - \nabla \cdot (\nu \nabla \mathbf{u}) + \nabla p = \mathbf{0}, \qquad \nabla \cdot \mathbf{u} = 0. \tag{A.19}$$

The computation of the interface flux is therefore performed by considering the linear hyperbolic system

$$\begin{aligned} &\frac{\partial p}{\partial t} + c^2 \frac{\partial u}{\partial x} = 0, \\ &\frac{\partial u}{\partial t} + \frac{\partial p}{\partial x} = 0. \end{aligned} \tag{A.20}$$

Notice that the equation for the tangential velocity component v has been neglected since it gives

$$\frac{\partial v}{\partial t} = 0 \quad \Rightarrow \quad v = \text{constant}.$$

The eigenvalues and eigenvectors of the associated matrix are the same as in the Navier–Stokes case (see Eq. A.4 and A.3) with the substitutions $u \leftarrow 0$ and, consequently, $a \leftarrow c$. We therefore have that $\lambda^S_\pm = \pm c$ and that the Riemann invariants $\Gamma^S_\pm$ are

$$\Gamma^S_\pm = p \pm cu.$$

The solution for u_* and p_* can be obtained by solving the system

$$\Gamma^S_+(u_*, p_*) = \Gamma^S_+(u_L, p_L), \qquad \Gamma^S_-(u_*, p_*) = \Gamma^S_-(u_R, p_R),$$

which gives

Table A.1
Solution of the Riemann problem for the tangential velocity component

sign(u_*)	Rarefaction	Shock
$u_* > 0$	$\mathbf{v}_* = \mathbf{v}_L \dfrac{u_L + a_L}{u_* + a_*}$	$\mathbf{v}_* = \mathbf{v}_L \dfrac{u_L - s_-}{u_* - s_-}$
$u_* < 0$	$\mathbf{v}_* = \mathbf{v}_R \dfrac{u_* + a_*}{u_R + a_R}$	$\mathbf{v}_* = \mathbf{v}_R \dfrac{u_R - s_+}{u_* - s_+}$

$$
\begin{aligned}
u_* &= \{u\} + \frac{1}{2c}[p], \\
p_* &= \{p\} + \frac{c}{2}[u].
\end{aligned}
\tag{A.21}
$$

As noticed above, in this case the third equation gives poor information on the tangential velocity component. This is, however, of no importance, since it is easy to realize that it never appears in the boundary terms.

The solution in the star region has a slightly more complex expression when considering the Oseen equations

$$
\begin{aligned}
&\frac{\partial \mathbf{u}}{\partial t} - \nabla \cdot (\nu \nabla \mathbf{u}) + \boldsymbol{\beta} \cdot \nabla \mathbf{u} + \nabla p = \mathbf{0}, \\
&\nabla \cdot \mathbf{u} = 0.
\end{aligned}
\tag{A.22}
$$

In this case, we have to solve the following linear hyperbolic system

$$
\begin{aligned}
&\frac{\partial p}{\partial t} + c^2 \frac{\partial u}{\partial x} = 0, \\
&\frac{\partial u}{\partial t} + \frac{\partial (\beta_{\mathbf{n}} u + p)}{\partial x} = 0, \\
&\frac{\partial v}{\partial t} + \frac{\partial (\beta_{\mathbf{n}} v)}{\partial x} = 0,
\end{aligned}
\tag{A.23}
$$

where $\beta_{\mathbf{n}}$ indicates the normal component of the advection velocity in the (quadrature) point where we are solving the Riemann problem. The eigenvalues are

$$
\lambda_{\pm} = \frac{\beta_{\mathbf{n}} \pm \alpha}{2}, \qquad \lambda_0 = \beta_{\mathbf{n}},
$$

being $\alpha \stackrel{\text{def}}{=} \sqrt{\beta_{\mathbf{n}}^2 + 4c^2}$. The Riemann invariants $\Gamma^O_{\pm,0}$ are

$$
\Gamma^O_{\pm} = p + \frac{1}{2}(\beta_{\mathbf{n}} \pm \alpha) u, \qquad \Gamma^O_0 = \beta_{\mathbf{n}} v.
$$

Notice that these expressions reduce to the Stokes case for $\beta_{\mathbf{n}} = 0$. The solution for the normal velocity component and the pressure in the star region can be obtained by solving the system

$$
\begin{aligned}
&\Gamma^O_+(u_*, p_*) = \Gamma^O_+(u_L, p_L), \\
&\Gamma^O_-(u_*, p_*) = \Gamma^O_-(u_R, p_R),
\end{aligned}
$$

which gives

$$
\begin{aligned}
u_* &= \{u\} + \frac{1}{\alpha}[p] + \frac{\beta_{\mathbf{n}}}{2\alpha}[u], \\
p_* &= \{p\} + \frac{c^2}{\alpha}[u] - \frac{\beta_{\mathbf{n}}}{2\alpha}[p].
\end{aligned}
\tag{A.24}
$$

Once again, Eq. (A.24) reduce to Eq. (A.21) when $\boldsymbol{\beta} = \mathbf{0}$. As regards the tangential velocity component, we have

$$
\Gamma^O_0(v_*) = \begin{cases} \Gamma^O_0(v_L) & \text{if } u_* > 0, \\ \Gamma^O_0(v_R) & \text{if } u_* < 0, \end{cases}
$$

or

$$
v_* = \begin{cases} v_L & \text{if } u_* > 0, \\ v_R & \text{if } u_* < 0, \end{cases}
$$

i.e. the tangential velocity component is always taken from the upwind side with respect to u_*.

References

[1] J.-G. Liu, C.-W. Shu, A high-order discontinuous Galerkin method for 2D incompressible flows, J. Comput. Phys. 160 (2000) 577–596.
[2] B. Cockburn, G. Kanschat, D. Schötzau, C. Schwab, Local discontinuous Galerkin methods for the Stokes system, SIAM J. Numer. Anal. 40 (1) (2002) 319–343.
[3] B. Cockburn, G. Kanschat, D. Schötzau, The local discontinuous Galerkin method for the Oseen equations, Math. Comp. 73 (246) (2003) 569–593.
[4] B. Cockburn, G. Kanschat, D. Schötzau, A locally conservative LDG method for the incompressible Navier–Stokes equations, Math. Comp. 74 (251) (2005) 1067–1095.
[5] F. Bassi, S. Rebay, A high-order accurate discontinuous finite element method for the numerical solution of the compressible Navier–Stokes equations, J. Comput. Phys. 131 (1997) 267–279.
[6] F. Bassi, S. Rebay, G. Mariotti, S. Pedinotti, M. Savini, A high-order accurate discontinuous finite element method for inviscid and viscous turbomachinery flows, in: R. Decuypere, G. Dibelius (Eds.), Proceedings of the 2nd European Conference on Turbomachinery Fluid Dynamics and Thermodynamics, Technologisch Instituut, Antwerpen, Belgium, 1997, pp. 99–108.
[7] D.N. Arnold, F. Brezzi, B. Cockburn, D. Marini, Unified analysis of discontinuous Galerkin methods for elliptic problems, SIAM J. Numer. Anal. 39 (5) (2002) 1749–1779.
[8] L.S.G. Kovasznay, Laminar flow behind a two-dimensional grid, Proc. Camb. Philos. Soc. 44 (1948) 58–62.
[9] U. Ghia, K.N. Ghia, C.T. Shin, High-*Re* solutions for incompressible flow using the Navier–Stokes equations and a multigrid method, J. Comp. Phys. 48 (1982) 387–411.
[10] O. Botella, R. Peyret, Benchmark spectral results on the lid-driven cavity flow, Comput. Fluids 27 (4) (1998) 421–433.
[11] E. Erturk, T.C. Corke, C. Gokcol, Numerical solutions of 2-D steady incompressible driven cavity flow at high Reynolds numbers, Int. J. Numer. Meth. Fluids 48 (2005) 747–774.
[12] D.A. Di Pietro, Discontinuous Galerkin methods for the incompressible Navier–Stokes equations, Ph.D. thesis, Università degli Studi di Bergamo, January 2006.
[13] R. Cools, An Encyclopædia of Cubature Formulas, J. Complexity 19 (2003) 445–453.
[14] S. Balay, K. Buschelman, W.D. Gropp, D. Kaushik, M.G. Knepley, L.C. McInnes, B.F. Smith, H. Zhang, PETSc Web page, <http://www.mcs.anl.gov/petsc>, 2001.
[15] D.T. Elsworth, E.F. Toro, Riemann solvers for solving the incompressible Navier–Stokes equations using the artificial compressibility method, College of Aeronautics Report 9208, Cranfield Institute of Technology, England, June 1992.